Fault Slip Rates, Effects of Sediments and the Strength of the Lower Crust in the Salton Trough Region, Southern California

Noah P. Fay and Eugene D. Humphreys
University of Oregon

Noah Fay
Department of Geological Sciences
University of Oregon
Eugene OR 97403
(541) 346-4653

nfay@uoregon.edu

Abstract

In southernmost California the Salton Trough sedimentary basin lies between the subparallel San Jacinto and San Andreas faults that together with the Elsinore fault accommodate ~ 80% of the 50 mm/yr of Pacific-North American relative motion. The slip rates on the San Andreas and San Jacinto faults have been a matter of recent debate and one source of uncertainty is the the influence of crustal strength heterogeneity due to elastcially weak basin sediments on geodetic data. To evalulate these effects we have modeled regional kinematics with elastic and viscoelastic finite element models which incoroporate laterally and vertically varying crustal material properties. We find that in general the effects of the sedimentary basin on surface deformation are relatively small and to explain the geodetic velocity data the slip rate on the San Andreas must be higher than that on the San Jacinto fault, consistent with traditional geologic estimates. We also conclude that a relatively high viscosity lower crust of $\geq 1\times10^{20}$ Pa-s lies beneath this region.

1.0 Introduction

In the Salton Trough region (Fig. 1) of southern California the subparallel San Jacinto, San Andreas and Elsinore faults together accommodate ~ 80% of the ~ 50 mm/yr of relative Pacific-North American motion [DeMets & Dixon, 1999]. A variety of geologic (e.g., paleoseismology, geomorphology) techniques have been used to estimate the long-term slip rates on these faults to assess the evolution of the plate-boundary fault system, regional kinematics and seismic hazard. 'Traditional' estimates suggest that the San Andreas is slipping at approximately twice the rate of the San Jacinto, i.e., approximately 25 and 12 mm/yr respectively, and the Elsinore is far less active at ~ 4 mm/yr [Keller et al., 1982; Weldon & Sieh, 1985; Rockwell et al., 1990; Petersen and Wesnousky, 1994; Humphreys & Weldon, 1994]. Reassessment of previous work [Dorsey, 2003], new geologic [Kendrick et al., 2002] and geodetic data [Johnson et al., 1994; Anderson et al., 2003] suggest a higher slip rate for the San Jacinto fault and a correspondingly slower San Andreas. Since geodetic data are instantaneous (in a geologic sense), a major goal of the community is to relate these geodetic data to long-term fault slip rates. This is often done through the use of simple elastic half-space [e.g., Savage & Burford, 1973; Feigl et al., 1993], or viscoelastic relaxation models [Savage & Prescott, 1978; Savage and Lisowski, 1998; Pollitz, 2001; Dixon et al., 2003].

Interseismic strain is naturally sensitive to the heterogeneous elastic and viscous properties of the lithosphere, complicating interpretation of geodetic observations [e.g., Malservisi et al., 2001]. The Salton Trough, which lies between the San Jacinto and San Andreas faults, is a thick sedimentary basin where strong variations in seismic velocity [Kohler et al., 2003; Magistrale et al., 2000] imply large crustal elastic moduli variations, and high heat flow [Lachenbruch et al., 1985; Bonner et al., 2003] suggests relatively low lower crust and

upper mantle viscosity. Previous work in the Ventura Basin of southern California [Donnellan et al., 1993; Hager et al., 1999] has shown that an elastically weak sedimentary cover can obscure locking depth and slip rates estimates based on geodetic data. Thus lateral and vertical variations in elastic and viscous properties in the Salton Trough may be important in influencing the form of surface deformation and therefore our interpretation of geodetic data.

In this paper we use two simple, kinematic earth models to estimate the contemporary slip rates of the San Andreas, San Jacinto and Elsinore faults, and the effects of variable elastic and viscous structure of the Salton Trough lithosphere. We have systematically modeled a number of elastic and viscoelastic crustal structures to determine the range of acceptable models. Our primary results are: (1) the effects of the elastically weak Salton Trough sedimentary basin on geodetic velocity are small, (2) models are most consistent with a higher San Andreas than San Jacinto fault slip rate, and (3) models require a fairly strong lower crust with minimum viscosity of 1×10^{20} Pa-s.

2.0 Geodetic data and shear modulus constraints

We use two data sets provided by the Southern California Earthquake Center to constrain our models. The Crustal Motion Map version 3.0 (CMM3) of Shen et al. [2003] is a compilation of various types of geodetic data (e.g., campaign GPS, continuous GPS, EDM) realized into a common North American reference frame, convenient for plate-boundary studies. The co- and post- seismic effects of recent southern California earthquakes (Landers, 1992; Northridge, 1994; Hector Mine, 1999) have been removed from the data as to best represent the interseismic velocity field [Shen et al., 2003].

We have selected a subset of the CMM3 to model the Salton Trough region. This subset includes all stations in a swath perpendicular to the relatively simple San Andreas fault excluding those whose motion may be strongly affected by slip transfer from the southern San Andreas fault system to the Eastern California Shear Zone. Figure 1a shows that the dominant orientations of the faults and most of the chosen velocity vectors are nearly parallel to that predicted by the Pacific-North American Euler pole [Demets & Dixon, 1999], indicating fault normal motion in this region is small. Thus we model only fault parallel velocity (Fig. 1b) in 2.5 dimensions, i.e., 2D cross-sections perpendicular to the faults with motion in the third dimension, parallel to the faults.

The stations near the San Jacinto fault shown in Figure 1 are separated into two groups. The fault-parallel velocities of the 'south' stations (open squares) are generally faster/slower than the 'north' stations (triangles) on the western/eastern side of the San Jacinto fault. This along-strike variation in shear strain rate probably reflects a transient process since block rotations are minimal at this latitude and long-term block motions are largely fault-parallel [Humphreys & Weldon, 1994].

Geodetic velocities are nearly indistinguishable from stable North America beyond ~ 45 km east of the San Andreas fault, although the small (~ 1 mm/yr) component of velocity in the San Andreas parallel direction is likely due to rotation of the Colorado plateau associated with extension in the Rio Grande Rift and southern Basin and Range [Humphreys & Weldon, 1994]. To account for this, we subtract 1 mm/yr, the approximate velocity of eastern California (east of the San Andreas fault) relative to North America resolved in the San Andreas fault parallel direction, from the velocity field shown in Figure 1. This 1 mm/yr represents relative Pacific-North American relative motion that is not associated with strike-slip plate boundary

deformation and should not be included in modeling so as to avoid overestimating fault slip rates. Crustal motion is nearly uniform at ~ 39 mm/yr beyond ~ 40 km west of the Elsinore fault although any strain accumulation on faults to the west of the data transect in Figure 1 (e.g., Rose Canyon, Newport-Inglewood) that we do not account for may cause a slight overestimate in slip rates. The low strain rate in the data (Fig. 1b), however, suggests this problem is minimal. Thus we have stable reference frame to the east of the San Andreas fault and low strain rate, coherent crustal movement west of the faults.

Shear strain rate is greatest over the San Andreas and San Jacinto faults (Fig. 1b). This concentration of strain was recognized early in central California and modeled as fault slip below a locking depth in a uniform elastic halfspace, which gives rise to the familiar 'arctangent' velocity field near strike-slip faults [Savage & Burford, 1973]. The magnitude of strain rate over a fault is thought to be indicative of the slip rate, though the covariance between locking depth and slip rate can sometimes make modeling geodetic data non-unique in this regard [e.g., Freymueller et al., 1999].

The three-dimensional Seismic Velocity Model, version 3 (SVM3) [Kohler et al., 2003; Magistrale et al., 2000] provides estimates of seismic velocity (V_p, V_s) and density (ρ) at any point in southern California lithosphere interpolated from a number of seismic velocity sources. We calculate space-varying shear modulus (μ) from V_s and ρ, (see Fig. 2). Models that incorporate the Salton Trough as an elastically distinct volume are based on the out-of-basin (black line in Fig. 2) and in-basin (dashed) shear modulus vs. depth profile. For our purposes, we define the basin as 20 km wide and adjacent to the San Andreas fault. Below ten kilometers it appears that the elastically weak basin sediments are compensated by the strong lower crust

(Fig. 2) thought to result from intrusive magmatism at this landward extension of the Gulf of California oceanic spreading system [Elders et al., 1972; Lachenbruch et al., 1985].

3.0 Techniques

Two methods have seen wide use in evaluating southern California geodetic data. Surface displacements due to fault slip in a uniform, elastic halfspace [Okada, 1985; 1992] have been used by many authors to invert geodetic data for long-term slip rates via a back-slip method that accounts for interseismic strain accumulation [e.g., Feigl et al., 1993; Bennett et al., 1996; McClusky et al., 2001; Becker et al., in print; Meade & Hager, in review]. This method implicitly assumes a high viscosity lithosphere, i.e., effectively elastic, such that time-dependent viscous processes are not important on the time scales of geodetic observations. The apparent success of this method to match most of the geodetic data in southern California [Meade & Hager, in review] suggests it captures the essence of surface kinematics in this region.

Surface deformation is also modeled using an elementary earthquake cycle on a fault embedded in an elastic layer overlying a Maxwell viscoelastic halfspace [Nur & Mavko, 1974; Savage & Prescott, 1978; Thatcher, 1983; Savage, 2000; Pollitz, 2001; Dixon et al., 2003]. The surface velocity near a fault predicted by this method depends on the thickness of the elastic layer, the viscosity structure of the viscoelastic substrate and time of observation within the earthquake cycle.

While the analytic solutions to the elastic halfspace and viscoelastic models are useful, they are limited to a relatively few simple cases with uniform or layered rheologies. We therefore use the finite element method that can accommodate arbitrarily complex elastic and viscoelastic rheologies, faults, and kinematic and dynamic boundary conditions. Finite elements

is a robust method and has been widely used to evaluate regional kinematics [e.g., Williams & Richardson, 1991; Saucier & Humphreys, 1993; Hearn et al., 1998], effects of variations in crustal strength and thickness [Hager et al., 1999; Schmalzle et al., 2003] and earthquake dynamics [e.g., Freed & Lin, 2001; Hearn, 2003]. Specifically, we use the finite element code TECTON [Melosh & Raefsky, 1980; Williams & Wadge, 2000], which is a linear-element, fully three-dimensional code that incorporates both elastic and Maxwell viscoelastic rheology. Below we compare finite element results to analytic solutions to verify the accuracy of the numerical method.

Faults are included in the finite element models in two ways. Slippery nodes [Melosh & Williams, 1989] allow surfaces to be free-slip, i.e., zero shear stress, while maintaining the fault surface. Earthquakes are included with the split node technique [Melosh & Raefsky, 1981] that imposes an instantaneous relative offset across a fault surface. This technique is commonly used in finite element earthquake displacements and post-seismic relaxation studies [e.g., Hearn, 2003]. The elastic and viscoelastic models, described in detail in the next section, use slippery and split nodes, respectively.

4. Models and Results

In this study we include two sets of kinematic models: the elastic locking depth/deep slip model, and viscoelastic earthquake cycle model. Below each are discussed in terms of set-up, specific calculations and results.

4.1 Elastic locking depth/deep slip model

Introduction

The locking depth/deep slip model is a kinematic description of crustal blocks sliding past on another accommodated by faults that slip continuously at the tectonic load rate below some locking depth, and are locked above. The locked portion of the fault releases the accumulated strain during great earthquakes. The locking depth is often assumed to be base of seismicity, approximately 15 km depth throughout much of southern California [e.g., Magistrale, 2002].

Our version of this model is shown in Figure 3. An elastic block of 30 km thickness (the approximate Moho depth [Zhu & Kanamori, 2000]) with slippery-node faults below a specified locking depth, is driven by moving the bottom nodes of each block into the page of Figure 3. Blocks are driven at the bottom because we find that side-driven models distribute shear strain much too broadly to reasonably match the high strain rates near faults observed in the geodetic data. The relative velocities imposed at the base of the blocks reflect the slip rates of the block-bounding faults. In this way we are able to forward model slip rate hypotheses and invert for the set of slip-rates that produces a velocity field that best matches the geodetic velocity data. Surface velocity resulting from a unit slip rate for each fault is shown in Figure 3. Note that the interseismic fault slip tapers from zero at the locking depth to full slip at the driving depth, whereas in the elastic halfspace models [Okada, 1985] faults slip uniformly from the locking depth to infinite depth.

To find the best fitting set of slip rates we adopt the standard least squares misfit minimization method by solving

$$a = (G^T W^{-1} G)^{-1} G^T W^{-1} d \,, \qquad (1)$$

where G is a Green's function matrix that contains surface velocity due to unit slip on each of the three faults, W is a diagonal weighting matrix, $W_{ii} = \sigma_i^2$, and σ_i is the standard deviation of the geodetic velocities contained in vector d.

These models are driven such that the bottom of each block move at the prescribed rate independent of the assigned locking depth. Slipping faults between blocks concentrate strain above the faults, though the effects reasonable changes in locking depth are generally small. Therefore in calculating the Green's function matrix G in (1), we set the locking depths to the approximate average maximum depth of seismicity [Magistrale, 2002] near the faults, i.e., 16, 14, and 10 km for the Elsinore, San Jacinto and San Andreas faults respectively. Some uncertainty in locking depth is included in estimating slip rate uncertainty.

Uncertainties on the best-fitting slip rates are estimated via a Monte Carlo technique that accounts for data and locking depth uncertainty. During each Monte Carlo sample, each data point is randomly sampled according to a normal distribution defined by it's variance, a randomly sampled set of locking depth Green's functions (in the range of +/- 2 km) is used to construct G, and the slip rates are found by equation (1). After 1000 samples the distribution of each slip rate is mapped out and we use their standard deviations (σ) as formal uncertainties. All the uncertainties reported in this paper are 1σ. A similar bootstrap technique produced nearly identical uncertainty estimates.

Results

The results of three models are shown in Figures 4 – 6. In each figure we show the surface velocity for a uniform crust, for an elastically heterogeneous crust and the difference between them. The best-fitting model (solid line) is compared to a hypothesized 'equal slip'

model (dashed line), which has the San Jacinto, San Andreas and Elsinore faults slipping at 18, 18, and 4 mm/yr, respectively.

Figure 4 shows the effects of a weak volume extending to 10 km depth. This is a simple representation of a sedimentary basin adjacent to the San Andreas fault (see Fig. 1). The effect of the weak volume is to increase the strain rate over the basin, and decrease the velocity near the San Andreas fault. However, the magnitude of this effect is small, $\leq$ 2 mm/yr.

Figure 5 shows the effect of a weak volume underlain by a strong volume. This model is a simple representation of the Salton Trough crustal structure where the middle and lower crust is mostly mafic intrusive rocks and the upper crust is sedimentary rock that has been deposited as this area extended. Again the strain rate over the weak zone is increased, although the magnitude is smaller than the previous model (Fig. 5) due the compensating effect of the strong zone at depth.

Figure 6 shows the effects of crustal shear modulus structure of Figure 2. This elastic structure generally increases in shear modulus with depth everywhere and varies laterally from within to outside the basin. As in the previous two figures, the effect of the basin is a slight increase the strain rate within the basin, a slight decrease in the velocity near to San Andreas fault, and a poorer fit to the geodetic data compared to the uniform elasticity model. We conclude from these models that the elasticity structure in the Salton Trough region has only minor influence on the geodetic velocity, and in fact any 'basin signal' is not obvious in the geodetic data. The best-fitting slip rates for the San Andreas, San Jacinto and Elsinore faults for the uniform elastic model are 21.4 +/- 0.5, 15.2 +/- 0.9 and 2.7 +/- 0.7 mm/yr, respectively.

The Monte Carlo approach used in estimating uncertainties naturally accounts for the covariance between the estimated model parameters. Figure 7 shows the negative covariance

between the estimated San Andreas and San Jacinto fault slip rates with contours of least-squares model misfit, i.e., reduced chi-square, $\chi^2_\nu = [\Sigma_i({}_d v_i - {}_m v_i)^2 / \sigma_i^2]/(n-p)$, where ${}_d v$ and ${}_m v$ are data and model velocities, σ is data uncertainty, n is number of data points and p is the number of model parameters, p = 3 for these models. The approximate 95% confidence region, based on an F-ratio statistic [e.g., Dixon et al., 2002], is shown with the thick contour.

4.2 The viscoelastic earthquake cycle model

Introduction

The second earth model considered is the elementary viscoelastic earthquake cycle [Savage & Prescott, 1978] where the faulted lithosphere is modeled as a vertical cut (the fault) through an elastic layer overlying a Maxwell viscoelastic halfspace. The time-dependent surface velocity depends on the thickness of the elastic layer H, the earthquake recurrence interval T and the time since the last earthquake compared to the Maxwell relaxation time $\tau_m = \eta/\mu$ where η and μ are the viscosity and shear modulus respectively. Pollitz [2001] derived modified earthquake cycle solutions with constant surface velocity at a finite distance from the fault, to simulate the earthquake cycle in a finite width shear zone. With this approach, the surface velocity of a deforming zone are a consequence of the constant velocity of the sides of the shear zone and periodic earthquakes on the fault followed by viscoelastic relaxation of the earthquake-caused stresses. The surface velocity is thus the sum of steady simple shear and periodic, time-decaying earthquake cycle perturbations, which make for arctangent-like velocity profiles near the faults.

The geodetic velocities ~ 45 km to the east of the San Andreas fault and ~ 45 km to the west of the Elsinore fault are nearly constant, indicating that, at least for the effectively

instantaneous velocity field of the CMM3, a large fraction of Pacific-North American shear at this latitude is accommodated within a finite width zone. These geodetic data alone however are insufficient to discriminate between the infinite [Savage & Prescott, 1978] and finite-width [Pollitz, 2001] earthquake cycle models because both predict zero strain rate at sufficient distances away from faults and the form of interseismic deformation, and therefore interpretation of the geodetic velocity data, near to the fault depends on the model assumed. We follow the Pollitz [2001] finite width shear zone approach in our models (described below) for three reasons. First, the elementary earthquake cycle of Savage and Prescott [1978] is 'driven' by periodic earthquakes on a fault in the elastic layer and relaxation of the viscoelastic substrate. While the source of the driving stress does not change the infinite-width earthquake cycle solutions [Savage, 2000], the superimposed simple shear and earthquakes of the finite-width model [Pollitz, 2001] is more intuitively appealing considering the largely passive role of fault rupture in accommodating far-field relative Pacific-North American motion. Second, the finite-width model assumes a very high viscosity, i.e., effectively infinite relaxation time compared to earthquake repeat time, so that viscous relaxation in the viscoelastic substrate outside the deforming zone is negligible and the surface velocity is constant. This seems a reasonable assumption for our study region where we expect a lower viscosity Salton Trough lithosphere compared to the non-deforming Colorado Plateau to the east and Peninsular Ranges and oceanic lithosphere to the west. Finally, the finite-width model is more convenient for numerical modeling, necessary for addressing heterogeneous material properties.

The model set-up and finite element mesh is shown in Figure 8. The previous set of elastic models show that the Elsinore fault plays a small role in the total slip budget, so for simplicity we have removed its surface velocity contribution by subtracting from the geodetic

velocity the predicted surface velocity due to the Elsinore fault with a slip rate of 2.7 mm/yr, and model only the San Jacinto and San Andreas faults. The elastic layer 45 km east of the SAF is held fixed to represent stable North America. The elastic layer 45 km west of the SJF is kinematically driven into the page. We find that models with shear zone half-width much greater than the 65 km used here distribute strain too broadly to reasonably match the geodetic data and conform to the above observation that away from the faults the crust is not significantly straining.

At periodic intervals T an earthquake occurs on a fault with offset Tv, where v is fault slip rate. The surface velocity is then calculated for a number of time steps following each earthquake. Since the calculations are linear for Newtonian rheology, we compute each fault response independently with unit slip rate and scale and sum these Green's functions to get the total velocity field. Results are shown after a sufficient number of earthquakes such that the system is cycle invariant, i.e., start-up elastic transients have decayed to negligible values [Hetland & Hager, 2003].

The average recurrence interval (T) for the southern San Andreas fault is estimated at ~215-260 years [e.g., Fumal et al., 2002; Shifflett et al., 2002; Working Group on California Earthquake Probabilities (Jackson et al.,), 1995], and ~260 years for the San Jacinto fault at Anza [Rockwell et al., 2003]. We use a 250 year recurrence interval for both faults and find that models with a possibly shorter San Jacinto repeat time do not significantly change our conclusions.

The last surface rupture of the Coachella segment of the San Andreas is estimated to be in the late 1600s [Sieh & Williams, 1990; Shifflett et al., 2002], slightly over three hundred years ago. The relatively long elapsed time since the last rupture suggests that the fault is quite late in

its earthquake cycle. The southern strands of the San Jacinto fault have seen a number of moderate magnitude historic earthquakes (Mw >= ~6.5) [e.g., Sanders, 1993] including the fairly recent M_w 6.7 Borrego Mountain rupture in 1968. To the north the Anza segment has been historically quiescent [Thatcher et al., 1975; Sanders & Kanamori, 1984] and is considered fairly late in its earthquake cycle [Rockwell et al., 2003]. We therefore approximate the San Jacinto as a single fault mid-way (50% with uncertainty of 30-70%) through its earthquake cycle.

Benchmark test

To confirm the accuracy of the finite element method we compare the model response of a single, right-lateral fault earthquake cycle to the analytic solutions of Pollitz [2001]. Figure 9 shows the numerical results are nearly identical to the analytic solutions and the largest difference is $\leq$ 5%. Dixon et al., [2002] and Malservisi et al., [2001] made similar comparisons and came to similar conclusions.

Results

Below we show two models with variable elasticity, each with a suite of lower crust and upper mantle viscosities to demonstrate how the surface velocity depends on both the elastic and viscous structure of the lithosphere, in particular the viscosity of the lower crust.

Figures 10-12 shows a model with uniform elasticity (μ = 30 GPa) except a low shear modulus zone (μ/2) adjacent to the San Andreas fault to approximate the weak sedimentary basin. The velocity profile is shown for the San Jacinto and San Andreas faults at 50 and 90%, respectively, of the way through their earthquake cycles. If the viscosity of the viscoelastic substrate (lower crust and upper mantle) is relatively small, i.e., small τ_m compared to the

earthquake repeat time T, any earthquake signal decays in a few decades and the velocity profile is a straight line with slope proportional to the distance between the shear zone boundaries, i.e., simple shear (Fig. 10,11). Figure 12 shows that the minimum viscosity of the lower crust to maintain any arctangent-like signal, especially late in the San Andreas fault earthquake cycle, is $\sim 1\times10^{20}$ Pa-s. In all cases the effect of the weak elastic basin is to increase the strain rate within the basin and decrease the velocity near to the San Andreas fault, though the effect is small, < 3 mm/yr.

Figures 13-15 show a similar model except the elasticity structure is given by the seismic velocity model shown in Figure 2. This model represents the elastic contrast between the basin and adjacent crust and a gradual increase of shear modulus with depth. The net effect of the weak Salton Trough basin adjacent to the San Andreas fault is to increase the strain rate over the basin and decrease it elsewhere.

The best fitting San Andreas and San Jacinto fault slip rates, for the high viscosity lower crust models of Figures 12 and 15, are found via equation (1). These viscoelastic models provide velocity as a function of time through the earthquake cycle and we find the best-fitting slip rates by solving (1) with Green's functions calculated with the San Andreas and San Jacinto faults 90 and 50%, respectively, of the way through their earthquake cycles.

Uncertainties on best-fitting slip rates are again estimated with a Monte Carlo approach, with uncertainty in earthquake recurrence of the San Jacinto fault included. During each Monte Carlo sample random noise is added to the geodetic data points according to their uncertainty, Green's functions for the San Jacinto fault is calculated with randomly selected times between 30-70% through its earthquake cycles to reflect our uncertainty in recurrence interval and time of observation within the earthquake cycle (the San Andreas fault is fixed at 90% of the way

through its cycle), and slip rates are calculated with (1). After 1000 samples, the slip rate distribution is mapped out and the standard deviation is reported as the formal uncertainty

To summarize, for lower crust viscosities < 1×10^{20} Pa-s (Figs. 10, 11, 13, 14) the velocity profile is a straight line and shows no arctangent-like signal near the faults. Only models with lower crustal viscosity ≥ 1×10^{20} Pa-s can reasonably match the data. In all cases the net effect of the weak elastic zone on the surface velocity is ≤ 3 mm/yr. The best fitting San Andreas and San Jacinto fault slip rates for the high viscosity, uniform elastic properties model (Figs. 12b, 15b) are 25.7 +/- 0.8 and 11.3 +/- 0.9 mm/yr, respectively. A contour plot of model misfit (centered on 25.7 and 11.3 mm/yr with minimum χ_ν^2 of 1.02) showing the negative covariance between the estimated slip rates for these models would look very similar to that given in Figure 7.

5.0 Discussion

Effect of the Salton Trough sedimentary basin

In both the elastic and viscoelastic models the effect of the relatively weak Salton Trough sedimentary basin is to increase the strain rate within the basin and decrease the surface velocity near the San Andreas Fault. The magnitude in all cases is ≤ 3 mm/yr. Moreover, in all models this effect of the basin is to decrease the overall fit to the geodetic velocity data, which do not show any obvious signal of a change in strain rate near the San Andreas or the western edge of the basin as the models predict. Two explanations seem likely.

First, our models have over-simplified the actual geometry of the basin and crustal rheology. The actual shape of the basin may be such that the effect of the near-surface weak sediments smaller than we have predicted with the simple basin geometry. This is certainly true

considering the width of the basin changes along strike of the San Andreas fault. We have assumed for this two dimensional modeling that the basin is a fixed width of 20 km, half the distance between the San Andreas and San Jacinto faults. Addressing a more realistic basin structure would also require a three dimensional model that includes slip on the Imperial fault and oblique spreading in the Brawley Seismic Zone.

Second, the stronger, presumably mafic, lower crust plays a more important role in canceling the weak upper crust sedimentary rocks than we have modeled, possibly due to the simplicity of the SVM3 within the basin that may over/underestimate the seismic velocity of the upper crustal sediments and lower crustal mafic rocks, respectively. In any case, the lack of obvious basin signal in the geodetic data implies the vertically integrated strength of basin crust is similar to crust outside the basin and the geodetic velocity in this strike-slip dominated region is more sensitive to this composite strength than any particular crustal component. Furthermore, the presence of the basin does not bias geodetic data significantly in a way that might explain the discrepant slip rate estimates for the San Jacinto and San Andreas faults.

Slip rates

The elastic and viscoelastic models consistently require a San Andreas fault slip rate greater than the San Jacinto fault, ~21 and 15 mm/yr for the elastic models and ~ 25 and 11 mm/yr for the viscoelastic models. These rates are consistent with the geologic estimates [e.g., Keller et al., 1982; Petersen & Wesnousky, 1994; Humphreys & Weldon, 1994], evolution of the plate boundary fault system [Powell & Weldon, 1992], and block models constrained by geodetic data [Bennett et al., 1996; Meade & Hager, in review; Becker et al., in print]. The higher San Jacinto rates suggested by Kendrick et al. [2002] and Dorsey [2003] are not

necessarily inconsistent considering our results reflect contemporary (and instantaneous) deformation and it appears the San Jacinto fault may have been much more active in the past [Bennett et al., 2004]. In addition, if the southern California fault system is abandoning the San Andreas in favor of the younger and more favorably aligned San Jacinto fault, as to avoid the energy expense of mountain building in the San Gorgonio pass area [e.g., Morton & Matti, 1993; Bennett et al., 2004], our results suggest this is not clearly evident in the contemporary geodetic data.

The difference in estimated slip rates between the two models (elastic and viscoelastic) can be understood in terms of the rupture history of the San Andreas fault and the time dependence of the viscoelastic earthquake cycle model. The surface velocity due to creep in an elastic halfspace (or our elastic models, Fig. 4-6) is approximately the same as the surface velocity due to a viscoelastic earthquake cycle model at approximately 50% of the way through the last cycle (for T = 250 yr. and $\mu = 1\times10^{20}$ Pa-s). Since the viscoelastic signal decays with time, and the San Andreas fault is well constrained to be (very) late in its cycle, a higher slip rate in the viscoelastic model is necessary to increase both the arctangent-like signal (slope) around the San Andreas and the magnitude of velocity between the San Andreas and San Jacinto faults. To satisfy block motion constraints, a higher San Andreas rate requires a correspondingly lower San Jacinto rate [Bennett et al., 2004].

Furthermore, models with a shorter San Jacinto fault recurrence interval or models earlier in the San Jacinto fault's cycle (or both) have the interesting effect of requiring a higher San Andreas slip rate. For example, being earlier in the San Jacinto earthquake cycle has the effect of increasing strain rate near the San Jacinto fault by accelerating the surface velocity to the west

of the fault and depressing it to the east (e.g., see Fig. 9); To match the magnitude of the velocities between the faults, the San Andreas rate must therefore be increased.

Johnson et al. [1994] and Anderson et al. [2003] analyzed geodetic data and found the shear strain rate near the San Jacinto fault to be similar to that of the San Andreas fault, suggesting similar slip rates. Our models slightly under fit the strain rate (i.e., spatial derivative of velocity profile) near to the San Jacinto fault. This can not be remedied by a much higher slip rate on the San Jacinto (e.g., 18 mm/yr), which would require a lesser San Andreas rate and cause significant misfit elsewhere, but can be explained in terms of earthquake related transient signals. As shown in Figure 1b, the fault-parallel surface velocities near the 1968 Borrego Mountain rupture are generally faster/slower on the western/eastern side of the San Jacinto fault, compared to stations to the north, consistent with the notion that the elevated strain rate is thus likely a transient signal associated with the recent earthquake. If true, the approximately steady [Anderson et al., 2003] and relatively long time-scale of post-seismic relaxation, compared with the rapid relaxation of the more recent Mojave Desert events [e.g., Freed & Bürgmann, 2004], suggests a more complicated rheology than the Maxwell viscosity we have assumed (see below).

High viscosity lower crust

Both the elastic and viscoelastic models require a high viscosity lower crust to match the geodetic data. The elastic halfspace deep slip method implicitly assumes a high viscosity, i.e., effectively elastic, rheology. The viscoelastic earthquake cycle models also require a lower crust viscosity of $\geq 1\times10^{20}$ Pa-s to maintain large velocity gradients near the faults late in the earthquake cycle.

Although the elastic halfspace and viscoelastic earthquake cycle surface velocity solutions converge in the high viscosity limit, and can't be differentiated based solely on geodetic data [Savage, 1990], we can eliminate the possibility that steady-state creep on faults in a relatively low viscosity lower crust and upper mantle cause the observed high velocity gradients at the surface. Analytic solutions [Zatman, 2000] and finite element modeling [Hetland & Hager, in press] have shown that an elastic layer overlying a linear viscoelastic halfspace is, in steady state, kinematically decoupled from the viscous substrate. This is to say, the steady-state surface velocity does not depend on velocities in the viscoelastic substrate [Hetland & Hager, in press], thus steady-state slip on a fault completely below the elastic layer (i.e., in the viscous lower crust and upper mantle) is not observable at the surface. Therefore, to explain the high surface velocity gradients with deep creeping faults, the faults must be creeping in the elastic upper crust or the high viscosity (effectively elastic) lower crust or upper mantle.

Heat flow in the southern Salton Trough region is very high [Lachenbruch et al., 1985; Bonner et al., 2003]. These high heat flow values, extensive hydrothermal activity and recent extrusive volcanism [e.g., Elders et al., 1972; Robinson et al., 1976] suggest high temperatures at depth. For example, Bonner et al., [2003] estimate 400°C at 10 km depth. Such high heat flow suggests a relatively low viscosity lower crust and upper mantle.

However, our results require a high viscosity lower crust, apparently in contradiction to these thermal arguments. The lower crust here is expected to be mafic in composition, a result of intrusive volcanism and underplating at the spreading center [e.g., Lachenbruch et al., 1985], and hence mineralogically stronger [Kohlstedt et al., 1995]. The lack of a significant gravity low over the low-density sedimentary basin rocks [Lachenbruch et al., 1985; Fuis et al., 1982] is consistent with a higher density, mafic, lower crust. Furthermore, since water and partial melt

content play an important role in controlling viscosity of mafic rocks [e.g., Hirth & Kohlstedt, 1996; Karato, 1986] and regional magmatism is no longer subduction related, we infer that the lower crust may also be dry and has little partial melt content, similar to Lachenbruch et al.'s [1985] conclusion that the crust is mostly solid. Thus the high viscosity of the lower crust probably derives from its dry, mafic composition.

For simplicity we have assumed a Newtonian viscosity lower crust and mantle though the high strain rate near the southern segment of the San Jacinto fault (see above) and post-seismic deformation studies of recent earthquakes in the Mojave desert, suggest that more complicated rheologies such as non-linear [Pollitz et al., 2001; Freed & Bürgmann, 2004] and linear composite viscosities [Ivins & Sammis, 1996; Ivins, 1996; Pollitz, 2003] are appropriate, or at least admissible, to describe southern California lithosphere. If true, we do not expect this would significantly change our earthquake cycle model conclusions; the lower crust would still have to be sufficiently high viscosity to retain high strain gradients late in the earthquake cycle. Moreover, the relatively rapid stress relaxation early in the cycle of a strain-rate dependent lower crust may require that the long-term viscosity be even higher than the $\sim 1 \times 10^{20}$ Pa-s we find, although this effect will be small if the earthquake related stresses are small compared to the background stresses in the strong lower crust.

Other studies of post-seismic relaxation following recent strike-slip earthquakes [e.g., Pollitz, 2003], subsidence due to surface loading of Lake Mead [Kaufmann & Amelung, 2000], and a general lack of significant earthquake-related transient signals in geodetic data throughout all of southern California [Meade & Hager, in review] also argue for a relatively high viscosity lower crust. These and our results suggest that the lower crust is an important component in the vertically integrated strength of the southern California lithosphere [e.g., Jackson, 2002].

6.0 Conclusions

We have investigated the effects of variable crustal rheology on surface deformation in the Salton Trough region of southern California with two simple kinematic finite element models. In general we find that the effect on surface velocity caused by the presence of the Salton Trough sedimentary basin is small and the geodetic velocity data are most consistent with a greater San Andreas than San Jacinto fault slip rate, approximately 23 and 13 mm/yr respectively. We also find that in order to explain the high gradients seen in the geodetic velocity data, the lower crust must have a minimum viscosity of $\sim 1\times10^{20}$ Pa-s.

Acknowledgements

This research was supported by the Southern California Earthquake Center and **NSF grant** ####. SCEC is funded by NSF cooperative Agreement EAR-0106924 and USGS Cooperative Agreement 02HQAG0008. The SCEC contribution number for this paper is XXXX. The figures in this paper were created with GMT [Wessel and Smith, 1991]. This work benefited greatly from discussions with Eric Hetland, Ray Weldon and Becky Dorsey. Reviews by

References

Anderson, G., D. C. Agnew and H. O. Johnson, Salton Trough regional deformation estimated from combined trilateration and survey-mode GPS data, *Bull. Seismol. Soc. Am., 93*, 2402-2414, 2003.

Armstrong, P. A. and D. S. Chapman, Beyond surface heat flow; an example from a tectonically active sedimentary basin, *Geology, 26*, 183-186, 1998.

Becker, T. W., Hardebeck, J. L., and G. Anderson, Constraints on fault slip rates of the southern California plate boundary from GPS velocity and stress inversions., submitted to *Geophys. J. Int.*

Bennett, R. A., W. Rodi and R. E. Reilinger, Global Positioning System constraints on fault slip rates in Southern California and northern Baja, Mexico, *J. Geophys. Res.,101*, 21,943-21,960, 1996.

Bennett, R. A., A. M. Friedrich and K. P. Furlong, Codependent histories of the San Andreas and San Jacinto fault zones from inversion of fault displacement rates, *Geology*, 32, 961-964, 2004.

Bonner, J. L., D. D. Blackwell and E. T. Herrin, Thermal constraints on earthquake depths in California, *Bull. Seismol. Soc. Am., 93*, 2333-2354, 2003.

DeMets, C. and T. H. Dixon, New kinematic models for Pacific-North America motion from 3 Ma to present; I, Evidence for steady motion and biases in the NUVEL-1A model, *Geophys.Res.Lett., 26*, 1921-1924, 1999.

Dixon, T., J. Decaix, F. Farina, K. Furlong, R. Malservisi, R. Bennett, F. Suarez-Vidal, J. Fletcher and J. Lee, Seismic cycle and rheological effects on estimation of present-day slip rates for the Agua Blanca and San Miguel-Valecitos faults, northern Baja California, Mexico, *J. Geophys. Res.,107*, 23, 2002.

Dixon, T. H., E. Norabuena and L. Hotaling, Paleoseismology and Global Positioning System; earthquake-cycle effects and geodetic versus geologic fault slip rates in the Eastern California shear zone, *Geology , 31*, 55-58, 2003.

Donnellan, A., B. H. Hager and R. W. King, Discrepancy between geological and geodetic deformation rates in the Ventura Basin, *Nature , 366*, 333-336, 1993.

Dorsey, R. J., Late Pleistocene slip rate on the Coachella Valley segment of the San Andreas Fault and implications for regional slip partitioning, Abstracts with Programs, Geological Society of America, 35(4), 22, 2003.

Elders, W. A., R. W. Rex, T. Meidav, P. T. Robinson and S. Biehler, Crustal Spreading in Southern California, *Science, 178*, 15-24, 1972.

Feigl, K. L., D. C. Agnew, Y. Bock, D. Dong, A. Donnellan, B. H. Hager, T. A. Herring, D. D. Jackson, T. H. Jordan, R. W. King, S. Larsen, K. M. Larson, M. H. Murray, Z. Shen and F. H. Webb, Space geodetic measurement of crustal deformation in Central and Southern California, 1984-1992, *J. Geophys. Res.,98*, 21,677-21,712, 1993.

Freed, A. M., and R. Bürgmann, R., Evidence of power-law flow in the Mojave desert mantle, *Nature*, 430, 548-551, 2004.

Freed, A. M. and J. Lin, Accelerated stress buildup on the southern San Andreas Fault and surrounding regions caused by Mojave Desert earthquakes, *Geology , 30*, 571-574, 2002.

Freymueller, J. T., M. H. Murray, P. Segall and D. Castillo, Kinematics of the Pacific-North America plate boundary zone, Northern California, *J. Geophys. Res.,104*, 7419-7441, 1999.

Fuis G. S., W. D. Mooney, J. H. Healey, G. A. McMechan and W. J. Lutter, Crustal structure of the Imperial Valley region, *U.S.Geol. Surv. Prof. Pap., 1254,* 25-49,1982.

Fumal, T. E., M. J. Rymer and G. G. Seitz, Timing of large earthquakes since A.D. 800 on the Mission Creek strand of the San Andreas fault zone at Thousand Palms Oasis, near Palm Springs, California, *Bull. Seismol. Soc. Am., 92*, 2841-2860, 2002.

Hager, B. H., G. A. Lyzenga, A. Donnellan and D. Dong, Reconciling rapid strain accumulation with deep seismogenic fault planes in the Ventura Basin, California, *J. Geophys. Res.,104*, 25,207-25,219, 1999.

Hearn, E. H., What can GPS data tell us about the dynamics of post-seismic deformation? *Geophys. J. Int., 155*, 753-777, 2003.

Hearn, E. H. and E. D. Humphreys, Kinematics of the southern Walker Lane Belt and motion of the Sierra Nevada block, California, *J. Geophys. Res.,103*, 27,033-27,049, 1998.

Hetland, E. A., and B. H. Hager, Interseismic Displacements: Cycle Invariance, Slip Rate and Rheology, *EOS Trans. AGU 84(46), G21B-0257*, 2003.

Hetland, E. A., and B. H. Hager, Relationship of geodetic velocities to velocities in the mantle, *Geophys. Res. Lett.*, in press.

Hirth, G. and D. L. Kohlstedt, Water in the oceanic upper mantle; implications for rheology, melt extraction and the evolution of the lithosphere, *Earth Planet.Sci.Lett., 144*, 93-108, 1996.

Humphreys, E. D. and R. J. Weldon, Deformation across the western United States: A local estimate of Pacific-North America transform deformation, *J. Geophys. Res*., 99, 19975-20010, 1994.

Ivins, E. R., Transient creep of a composit lower crust 2. A polymineralic basis for rapidly evolving postseismic deformation models, *J. Geophys. Res.,*101, 28,005-28,028, 1996.

Ivins, E. R. and C. G. Sammis, Transient creep of a composit lower crust 1. Constituitive theory, *J. Geophys. Res.,*101, 27,981-28,004, 1996.

Jackson, D. D., K. Aki, C. A. Cornell, J. H. Dieterich, T. L. Henyey, M. Mahdyiar, D. Schwartz and S. N. Ward, Seismic hazards in Southern California; probable earthquakes, 1994 to 2024, *Bull. Seismol. Soc. Am., 85*, 379-439, 1995.

Jackson, J., Strength of the continental lithosphere; time to abandon the jelly sandwich? *GSA Today, 12*, 4-10, 2002.

Johnson, H. O., D. C. Agnew and F. K. Wyatt, Present-day crustal deformation in Southern California, *J. Geophys. Res., 99*, 23,951-23,974, 1994.

Karato, S., Does partial melting reduce the creep strength of the upper mantle? *Nature, 319*, 309-310, 1986.

Kaufmann, G., and F. Amelung, Reservoir-induced deformation and continental rheology in vicinity of Lake Mead, Nevada, *J. Geophys. Res.*, 105, 16341-16358, 2000.

Keller, E. A., M. S. Bonkowski, R. J. Korsch and R. J. Shlemon, Tectonic geomorphology of the San Andreas fault zone in the southern Indio Hills, Coachella Valley, California, *Geological Society of America Bulletin, 93*, 46-56, 1982.

Kendrick, K. J., D. M. Morton, S. G. Wells and R. W. Simpson, Spatial and temporal deformation along the northern San Jacinto Fault, Southern California; implications for slip rates, *Bull. Seismol. Soc. Am., 92*, 2782-2802, 2002.

Kohler, M. D., H. Magistrale and R. W. Clayton, Mantle heterogeneities and the SCEC reference three-dimensional seismic velocity model version 3, *Bull. Seismol. Soc. Am., 93*, 757-774, 2003.

Kohlstedt, D. L., B. Evans, and S. J. Mackwell, Strength of the lithosphere: Constraints imposed by laboratory experiments, *J. Geophys. Res*., 100, 17587-17602, 1995.

Lachenbruch, A. H., J. H. Sass and S. P. Galanis Jr, Heat flow in southernmost California and the origin of the Salton Trough, *J. Geophys. Res., 90*, 6709-6736, 1985.

Magistrale, H., Relative contributions of crustal temperature and composition to controlling the depth of earthquakes in Southern California, *Geophys.Res.Lett., 29*, 4-7, 2002.

Magistrale, H., S. M. Day, R. Clayton and R. W. Graves, The SCEC Southern California 3D seismic velocity model Version 2, *Bull. Seismol. Soc. Am., S65-S76*, 216, 2000.

Malservisi, R., K. P. Furlong and T. H. Dixon, Influence of the earthquake cycle and lithospheric rheology on the dynamics of the eastern California shear zone, *Geophys.Res.Lett., 28*, 2731-2734, 2001.

McClusky, S. C., S. C. Bjornstad, B. H. Hager, R. W. King, B. J. Meade, M. M. Miller, F. C. Monastero and B. J. Souter, Present day kinematics of the eastern California shear zone from a geodetically constrained block model, *Geophys.Res.Lett., 28*, 3369-3372, 2001.

Meade, B. J., and B. H. Hager, Block Models of Crustal Motion in Southern California Constrained by GPS Measurements, submitted to *J. Geophys. Res*.

Melosh, H. J. and A. Raefsky, A simple and efficient method for introducing faults into finite element computations, *Bull. Seismol. Soc. Am., 71*, 1391-1400, 1981.

Melosh, H. J. and A. Raefsky, The dynamical origin of subduction zone topography, *Geophys. J. Roy. Astr. Soc., 60*, 333-354, 1980.

Melosh, H. J. and C. A. Williams Jr, Mechanics of graben formation in crustal rocks; a finite element analysis, *J. Geophys. Res.,94*, 13,961-13,973, 1989.

Morton, D. M. and J. C. Matti, Extension and contraction within an evolving divergent strike-slip fault complex; the San Andreas and San Jacinto fault zones at their convergence in Southern California, *The San Andreas Fault System; Displacement, Palinspastic Reconstruction, and Geologic Evolution Memoir - Geological Society of America, 178*, 217-230, 1993.

Nur, A. and G. Mavko, Postseismic Viscoelastic Rebound, *Science, 183*, 204-206, 1974.

Okada, Y., Internal deformation due to shear and tensile faults in a half-space, *Bull. Seismol. Soc. Am., 82*, 1018-1040, 1992.

Okada, Y., Surface deformation due to shear and tensile faults in a half-space, *Bull. Seismol. Soc. Am., 75*, 1135-1154, 1985.

Petersen, M. D. and S. G. Wesnousky, Fault slip rates and earthquake histories for active faults in Southern California, *Bull. Seismol. Soc. Am., 84*, 1608-1649, 1994.

Pollitz, F. F., Viscoelastic shear zone model of a strike-slip earthquake cycle, *J. Geophys. Res.,106*, 26,541-26,560, 2001.

Pollitz, F. F., Transient rheology of the uppermost mantle beneath the Mojave Desert, California, *Earth Planet. Sci. Lett.,*215, 89-104, 2003.

Pollitz, F. F., C. Wicks and W. Thatcher, Mantle flow beneath a continental strike-slip fault; postseismic deformation after the 1999 Hector Mine earthquake, *Science, 293*, 1814-1818, 2001.

Powell, T. E., and R. J. Weldon, Evolution of the San Andreas fault, *Annu. Rev. Earth Planet. Sci., 20,* 431-468, 1992.

Robinson, P. T., W. A. Elders and L. J. P. Muffler, Quaternary volcanism in the Salton Sea geothermal field, Imperial Valley, California, *Geological Society of America Bulletin, 87*, 347-360, 1976.

Rockwell, T.K., Loughman, C., and P. Merifield, Late Quaternary rate of slip along the San Jacinto fault zone near Anza, southern California: *J.Geophys. Res.,* 95, 8593-8605, 1990.

Rockwell, T. K., Young, J., Seitz, G., Meltzner, A., Verdugo, D., Khatib, F., Ragona, D., Altangerel, O., and J. West, 3,000 Years of Ground-rupturing Earthquakes in the Anza Seismic Gap, San Jacinto Fault, Southern California: Time to Shake It Up?, *Seism. Res. Lett.*, 74, 236-237, 2003.

Sanders, C. O., Interaction of the San Jacinto and San Andreas Fault Zones, Southern California: Triggered Earthquake Migration and Coupled Recurrence Intervals, *Science*, 260, 973-976, 1993.

Sanders, C. O., and H. Kanamori, A Seismotectonic Analaysis of the Anza Seismic Gap, San Jacinto Fault Zone, Southern California, *J. Geophys. Res*., 89, 5873-5890, 1984.

Saucier, F. and E. Humphreys, Horizontal crustal deformation in Southern California from joint models of geologic and very long baseline interferometry measurements, *Contributions of Space Geodesy to Geodynamics; Crustal Dynamics Geodynamics Series, 23*, 139-176, 1993.

Savage, J. C., Viscoelastic-coupling model for the earthquake cycle driven from below, *J. Geophys. Res.,105*, 25,525-25,532, 2000.

Savage, J. C. and R. O. Burford, Geodetic Determination of Relative Plate Motion in Central California, *J.Geophys. Res., 78*, 832-845, 1973.

Savage, J. C. and M. Lisowski, Viscoelastic coupling model of the San Andreas Fault along the big bend, Southern California, *J. Geophys. Res.,103*, 7281-7292, 1998.

Savage, J. C. and W. H. Prescott, Asthenosphere readjustment and the earthquake cycle, *J. Geophy.l Res., 83*), 3369-3376, 1978.

Schmalzle, G. M., Malservisi, R., and T. Dixon, Effects of Lateral Heterogeneity on Strain Accumulation Across the Carrizo Plain Segment of the San Andreas Fault, *EOS Trans. AGU 84(46), G31B-0705*, 2003.

Shen, Z. K., Agnew, D. C., King, R. W., Dong, D., Herring, T. A., Wang, M., Johnson, H., Anderson, G., Nikolaidis, R., van Domselaar, M., Hudnut, K. W., and D. D. Jackson, The SCEC Crustal Motion Map, Version 3.0, online at http://epicenter.usc.edu/cmm3/, 2003.

Shifflett, H., M. G. Gray, R. Grannell and B. L. Ingram, New evidence on the slip rate, renewal time, and late Holocene surface displacement, southernmost San Andreas Fault, Mecca Hills, California, *Bull. Seismol. Soc. Am., 92*, 2861-2877, 2002.

Sieh, K. E. and P. L. Williams, Behavior of the southernmost San Andreas Fault during the past 300 years, *J. Geophys. Res.,95*, 6629-6645, 1990.

Thatcher, W., Nonlinear strain buildup and the earthquake cycle on the San Andreas Fault, *J. Geophys. Res., 88*, 5893-5902, 1983.

Thatcher, W., Hileman, J. A., and T. C. Hanks, Seismic Slip Distribution along the San Jacinto Fault Zone, Southern California, and Its Implications, *Geol. Soc. Am. Bull., 86*, 1140-1146, 1975.

Weldon, R. J.,II and K. E. Sieh, Holocene rate of slip and tentative recurrence interval for large earthquakes on the San Andreas Fault, Cajon Pass, Southern California, *Geol. Soc. Am. Bull., 96*, 793-812, 1985.

Weldon, R., Scharer, K., Fumal, T., and G. Biasi, Wrightwood and the earthquake cycle: What a long recurrence record tells us about how faults work, *GSA Today, 14,* 4-10, 2004.

Wessel, P., and W. H. F. Smith, Free software helps map and display data, *EOS Trans. AGU, 84,* 441, 1991.

Williams, C. A. and R. M. Richardson, A rheologically layered three-dimensional model of the San Andreas Fault in Central and Southern California, *J. Geophys. Res.,96*, 16,597-16,623, 1991.

Williams, C. A. and G. Wadge, An accurate and efficient method for including the effects of topography in three-dimensional elastic models of ground deformation with applications to radar interferometry, *J. Geophys. Res.,105*, 8103-8120, 2000.

Zatman, S., On steady rate coupling between an elastic upper crust and a viscous interior, *Geophys. Res. Lett., 27*, 2421-2424, 2000.

Zhu, L. and H. Kanamori, Moho depth variation in Southern California from teleseismic receiver functions, *J. Geophys. Res.,105*, 2969-2980, 2000.

Figure Captions

Figure 1
(a) Map of study area shown in an Oblique Mercator projection about the Pacific-North American Euler pole of DeMets & Dixon [1999]. Geodetic station locations of the CMM3 (plus) and the subset used in this study (circle, triangle, open square). Velocities are shown in a North America reference frame and with 95% confidence ellipses [Shen et al., 2003]. Stations near the San Jacinto fault (SJF) are separated into two groups (triangles and open squares), see text and (b). Black lines show fault traces (SAF, San Andreas fault; ELS, Elsinore fault) and the stippled region represents the approximate location of the Salton Trough sedimentary basin as defined by the SVM3 [Kohler et al., 2003]. Note that the faults and the majority of the velocity vectors are subparallel Pacific-North American relative motion direction, indicating that crustal motion in this region is dominantly fault-parallel.

(b) Pacific-North American parallel surface velocity relative to North America. Grey bars show approximate fault locations. The San Jacinto fault 'south' and 'north' stations are shown with open squares and triangles, respectively, to emphasize the apparent along-strike variation in shear strain rate.

Figure 2
Shear modulus along cross section A-A' calculated from seismic velocity and density from SVM3 [Kohler et al., 2003]. Thin, grey lines show shear modulus-depth profiles for 81 positions along A-A' outside the Salton Trough basin (the basin is defined as 20 km wide and adjacent to the San Andreas fault) and their mean is given as the solid line. SVM3 is paramaterized such that any point (in map view) within the basin is assigned the same velocity-depth profile and the basin shear modulus structure is shown with the dashed line. Models that use this elasticity structure are thus based on two velocity-depth curves: points inside/outside the basin are assigned according to the dashed/solid line.

Figure 3
Elastic locking depth model used in Figures 4-6. Blocks are driven at the bottom to reflect the slip rates of the block-bounding faults. Surface velocity (solid line) is shown for 1 mm/yr on each fault (with equal locking depths of 14 km). The finite element mesh contains 3131 nodes and 3000 quadrilateral elements.

Figure 4
Elastic locking depth model results. (a) Model set-up cross-section showing free-slip faults (solid heavy lines), locked faults (dashed heavy lines), finite element mesh (thin lines; half of the total elements are shown for clarity), and elastic structure for the weak zone model. The model is driven as shown in Figure 3. (b) Map view velocity profile for the uniform elastic properties case showing data (dots with 1σ error bars), best-fitting model (solid line) with slip rates and 1σ uncertainties as labeled, and "equal slip" model (ELS = 4, SJF = 18, SAF = 18 mm/yr; dashed line). Light grey bars show fault locations. (c) Same as (b) except weak zone elasticity structure of (a). (d) The effects of the weak zone shown as the difference between the weak zone model and the uniform model (i.e., panel (c) – panel (b)).

Figure 5
Same as Figure 4 except the near-surface weak sediments are compensated by a strong zone at depth, which reduces the effect of the basin (d) on the surface velocity.

Figure 6
Same as Figure 4 except shear modulus according to Figure 2. Again the compensating effect of the strong volume at depth reduces the basin signal (d) at the surface compared to Figure 4.

Figure 7
Contours of model misfit χ^2_ν with respect to estimated slip rates of the San Andreas and San Jacinto faults. Star shows best fit ($\chi^2_\nu = 0.99$) and the thick line the approximate 95% confidence region.

Figure 8
Viscoelastic earthquake cycle model set-up and finite element mesh. The elastic upper crust (UC) is underlain by the lower crust (LC) underlain by the effectively semi-infinite upper mantle (UM). The two strike slip faults (solid lines in upper crust) are separated by 40 km, the approximate distance between the San Jacinto and San Andreas faults. The model is driven by holding the upper crust fixed to the right of the San Andreas fault and driving the upper crust left of the San Jacinto fault into the page. The bottom, right and left sides (below the elastic upper crust) are free. The dashed line shows the location of the fault used for the benchmarking exercise of Figure 8. The mesh contains 949 nodes and 892 quadrilateral elements.

Figure 9
Comparison of a finite element model (solid line) and analytic (Pollitz, 2001; dashed line) for a symmetric, finite-width shear zone earthquake cycle. The right-lateral fault with unit slip-rate cuts an elastic layer (15 km) which overlies a viscoelastic halfspace of viscosity (a) 1×10^{19} Pa·s and (b) 1×10^{20} Pa·s. Surface velocity is shown for a number of times (t) during the earthquake cycle as fractions of the earthquake repeat time T (250 yrs). The half-width of the shear zone is 65 km, and beyond 65 km the velocity is constant. The finite element results shown here were calculated with the same mesh used in actual modeling, see Figure 7. The largest difference between the numerical and analytic results is early in the earthquake cycle and approximately 5%.

Figure 10
Viscoelastic earthquake cycle model results. (a) Cross section showing fault locations (thick lines in upper crust) layered viscosity and elasticity structure, including a weak zone adjacent to the San Andreas fault (SAF). (b) Map view of velocity data (dots with 1σ uncertainty) and uniform upper crust earthquake velocity profile. (c) Weak zone model with weak elastic zone shown in (a). (d) Effect of the weak zone shown as the difference between the weak zone model and the uniform model, i.e., panel (c) – panel (b).

Figure 11
Same as Figure 9 with viscosity as shown. Note that the viscosity of the upper mantle differs by an order of magnitude, compared with Figure 10, and the velocity fields are nearly identical. This indicates the lower crust viscosity is the dominant control on surface velocity during the earthquake cycle.

Figure 12
Same as Figure 9 with viscosity as shown and best fitting slip rates with 1σ uncertainty. A minimum viscosity of 1×10^{20} Pa-s is necessary to retain any arctangent-like signal late in the earthquake cycle.

Figure 13
Viscoelastic earthquake cycle model results with weak zone model elastic structure according to SVM3, see Figure 2. (a) Cross section showing fault locations (thick lines in upper crust) layered viscosity and elasticity structure. (b) Map view of velocity data (dots with 1σ uncertainty) and uniform upper crust earthquake velocity profile. (c) Weak zone model using elastic structure of Figure 2. (d) Effect of the weak zone shown as the difference between the weak zone model and the uniform model, i.e., panel (c) – panel (b).

Figure 14
Same as Figure 12 with viscosity as shown. The 1×10^{19} Pa-s lower crust relaxes any earthquake stresses within a few decades such that the velocity profile is a straight line a few decades after the last earthquake.

Figure 15
Same as Figure 12 with viscosity as shown and best fitting slip rates with 1σ uncertainty. Again a high viscosity of 1×10^{20} Pa-s is necessary to reasonably match the data.

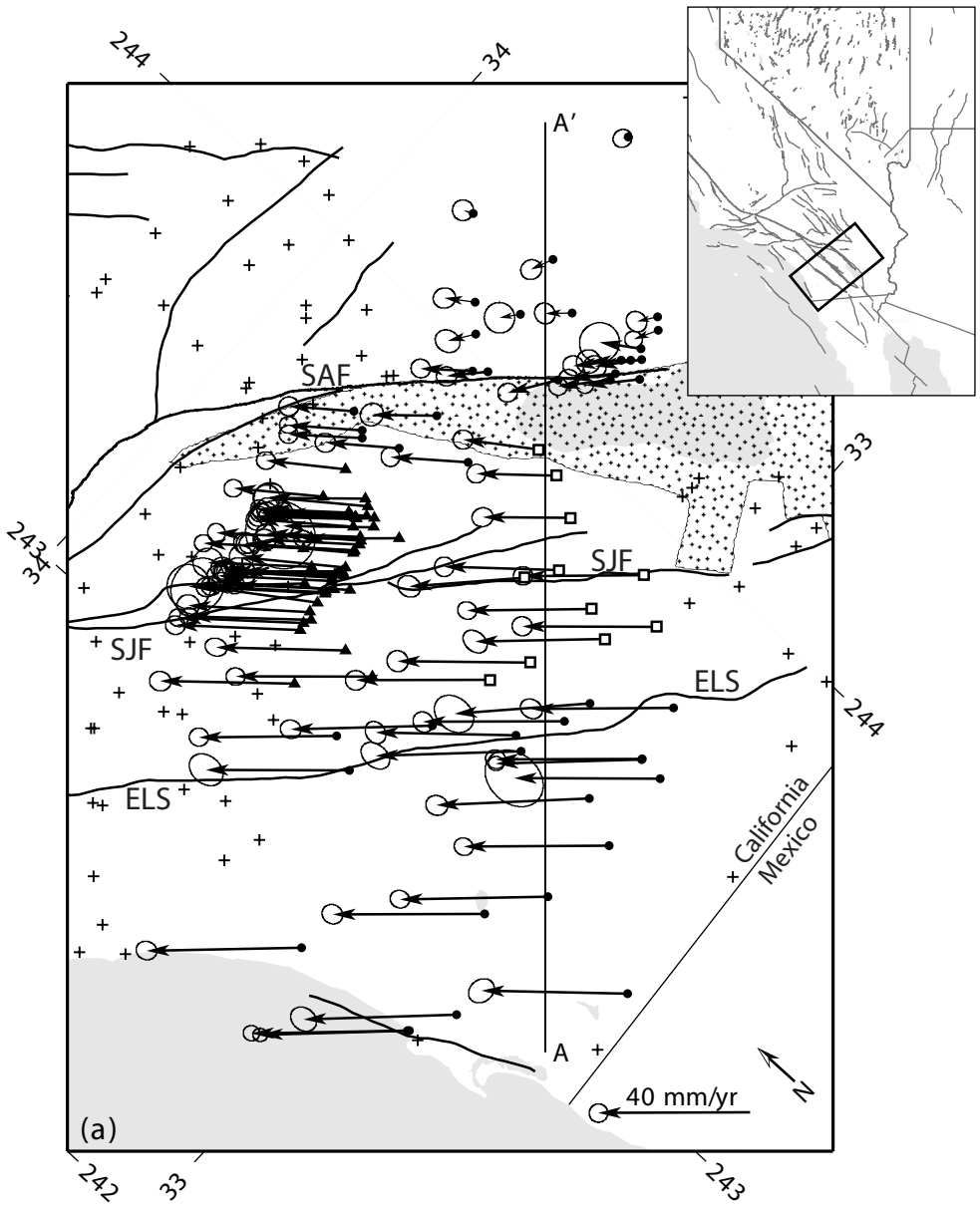
244
34
A′
SAF
33
243
34
SJF
SJF
ELS
244
ELS
California
Mexico
A
40 mm/yr
N
(a)
242
33
243

Figure 1a

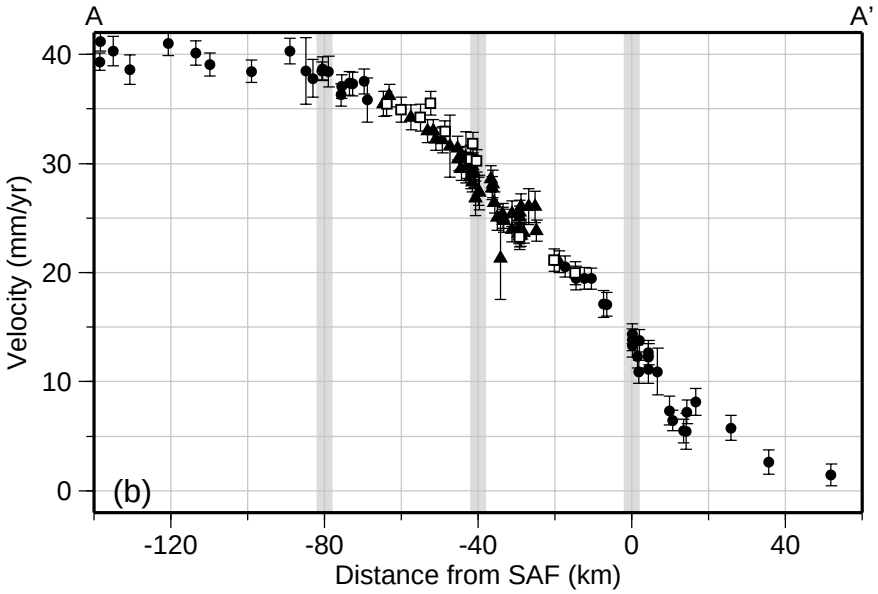
A
A'
40
30
20
10
0
Velocity (mm/yr)
(b)
-120
-80
-40
0
40
Distance from SAF (km)

Figure 1b

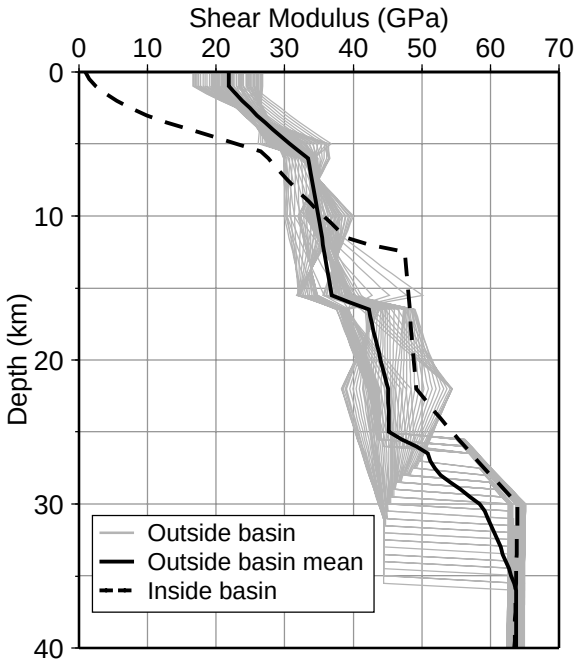
Shear Modulus (GPa)
0
10
20
30
40
50
60
70
Depth (km)
0
10
20
30
40
Outside basin
Outside basin mean
Inside basin

Figure 2

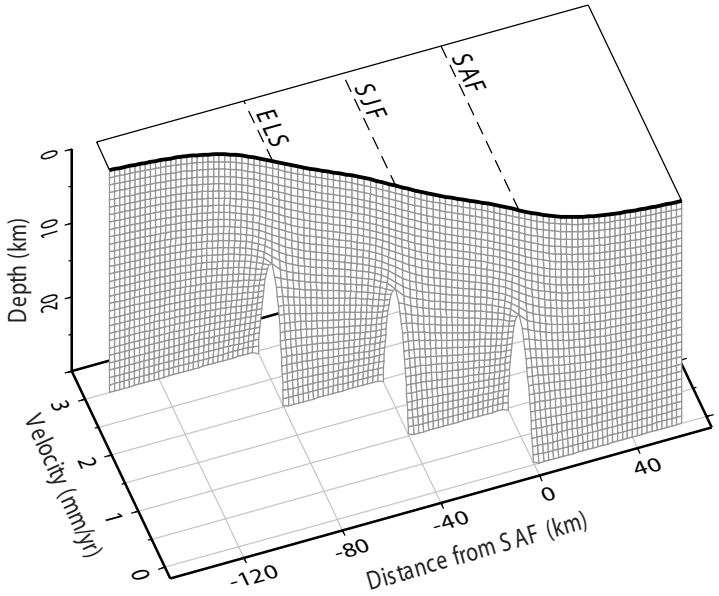
ELS
SJF
SAF
Depth (km)
0
10
20
Velocity (mm/yr)
3
2
1
0
-120
-80
-40
0
40
Distance from SAF (km)

Figure 3

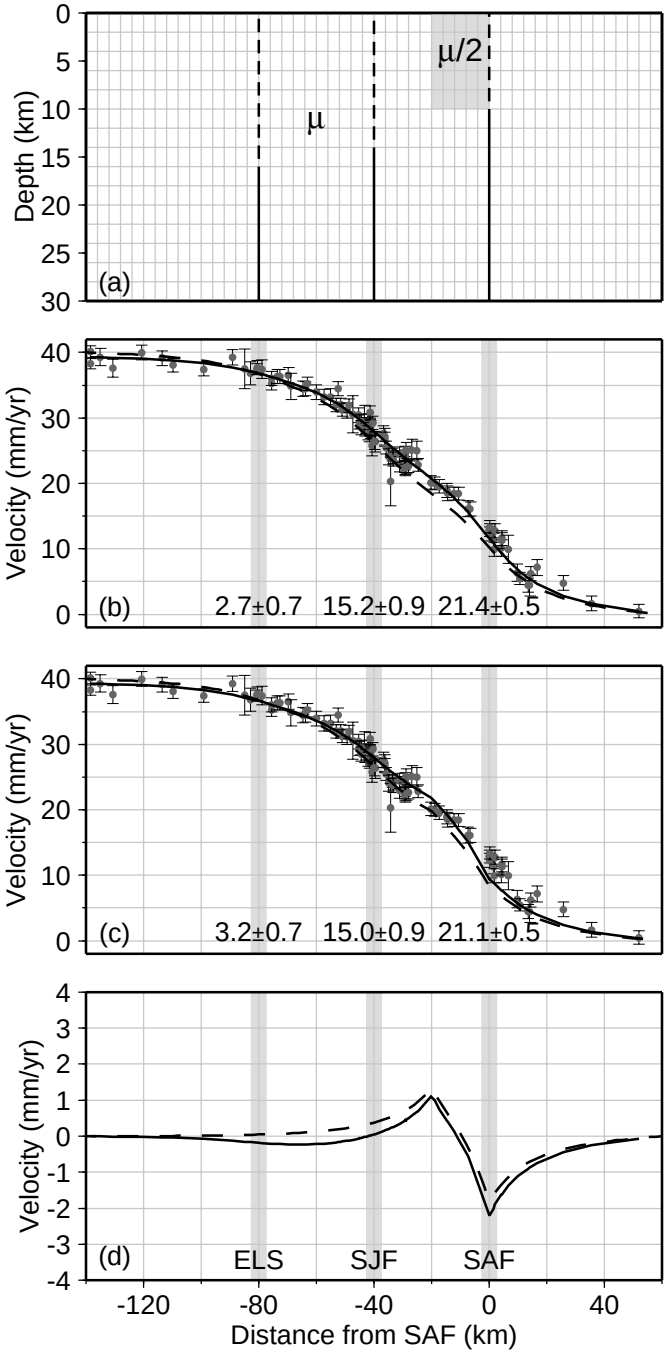
Depth (km)
μ
μ/2
(a)
Velocity (mm/yr)
(b)
2.7±0.7
15.2±0.9
21.4±0.5
Velocity (mm/yr)
(c)
3.2±0.7
15.0±0.9
21.1±0.5
Velocity (mm/yr)
(d)
ELS
SJF
SAF
Distance from SAF (km)

Figure 4

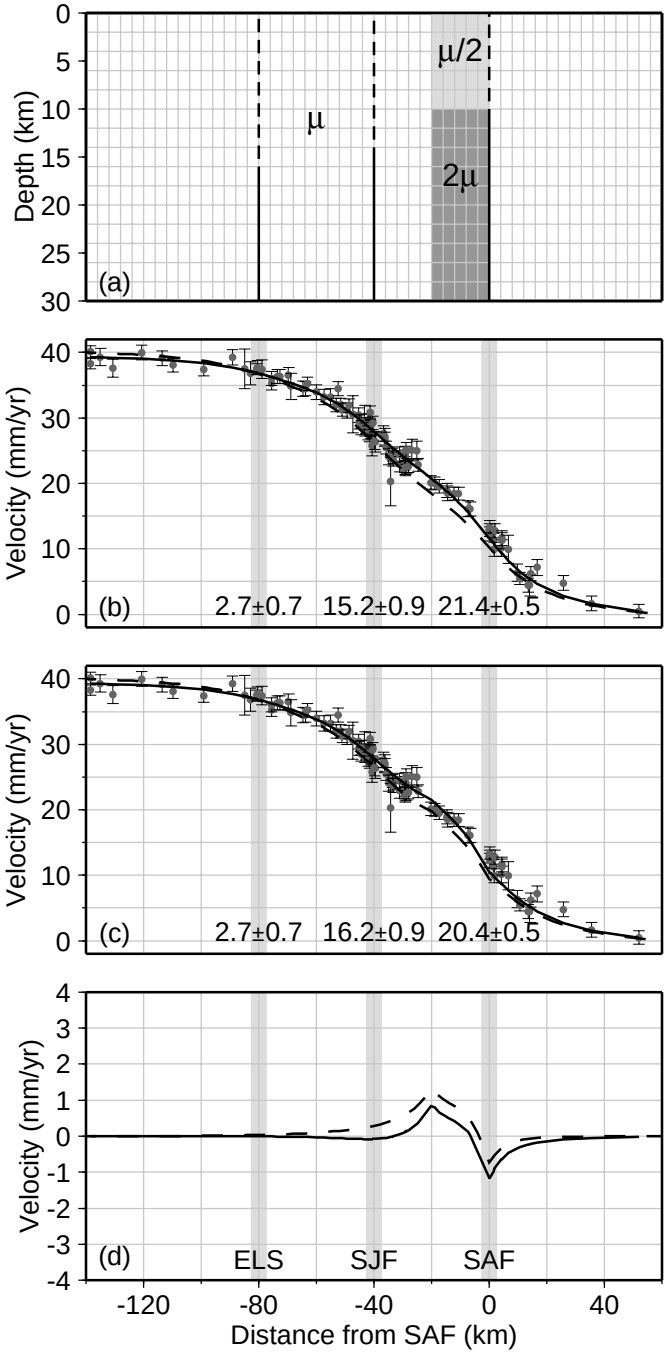
Depth (km)
μ/2
μ
2μ
(a)
Velocity (mm/yr)
(b)
2.7±0.7
15.2±0.9
21.4±0.5
Velocity (mm/yr)
(c)
2.7±0.7
16.2±0.9
20.4±0.5
Velocity (mm/yr)
(d)
ELS
SJF
SAF
Distance from SAF (km)

Figure 5

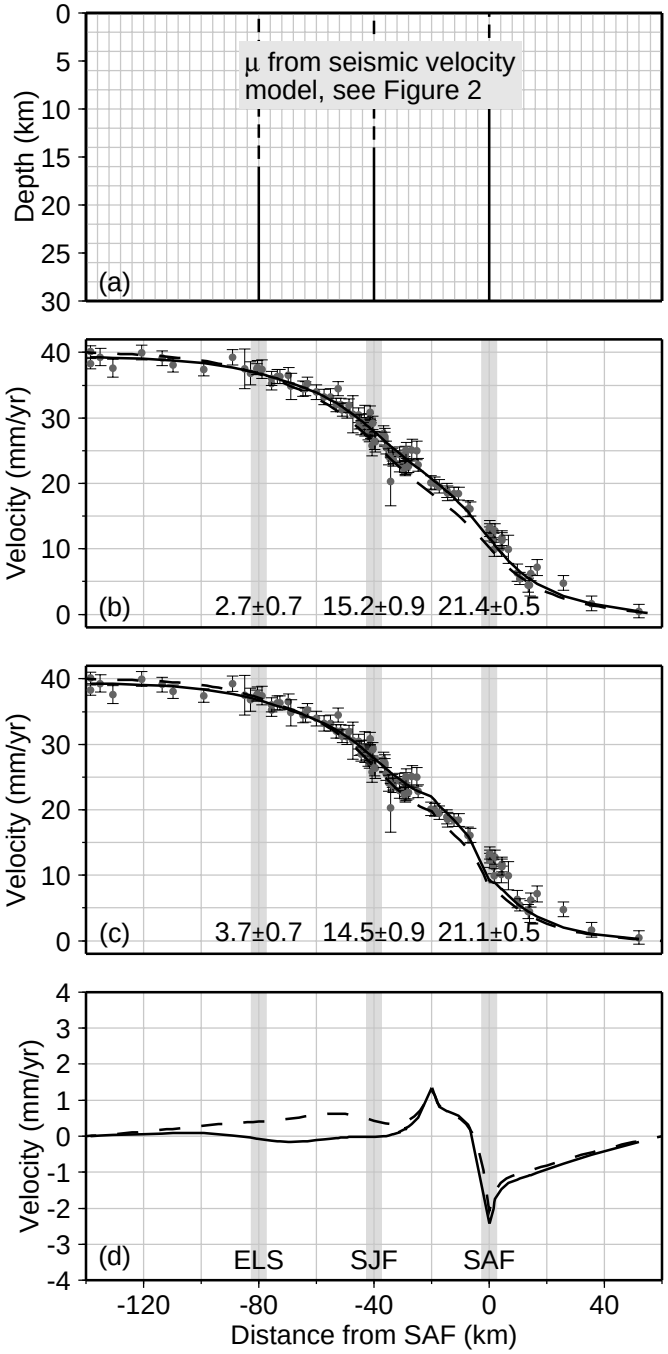
μ from seismic velocity model, see Figure 2
Depth (km)
(a)
Velocity (mm/yr)
(b)
2.7±0.7
15.2±0.9
21.4±0.5
Velocity (mm/yr)
(c)
3.7±0.7
14.5±0.9
21.1±0.5
Velocity (mm/yr)
(d)
ELS
SJF
SAF
Distance from SAF (km)

Figure 6

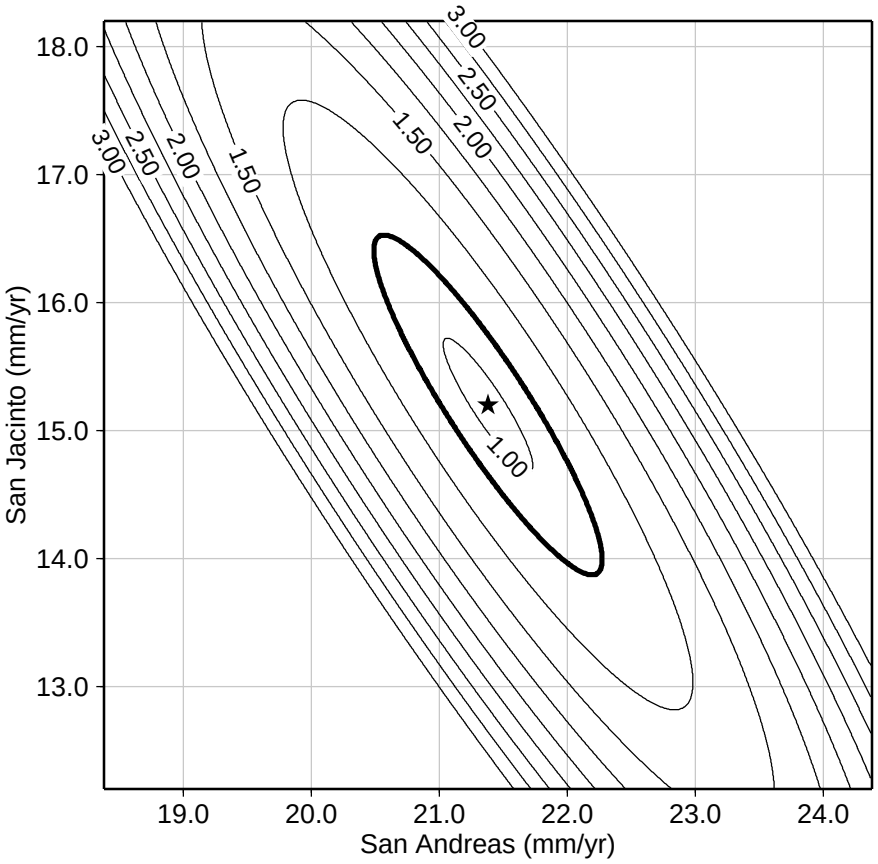
3.00
2.50
2.00
1.50
1.00
18.0
17.0
16.0
15.0
14.0
13.0
San Jacinto (mm/yr)
19.0
20.0
21.0
22.0
23.0
24.0
San Andreas (mm/yr)

Figure 7

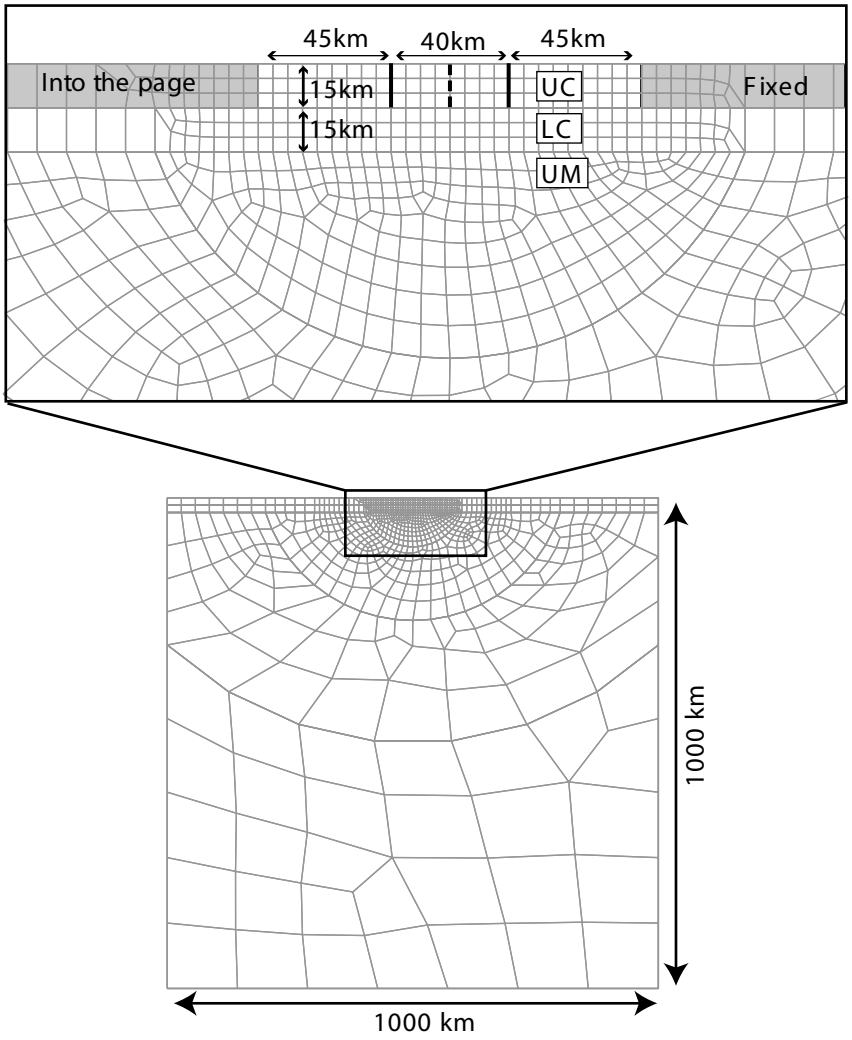
45km
40km
45km
Into the page
15km
15km
UC
LC
UM
Fixed
1000 km
1000 km

Figure 8

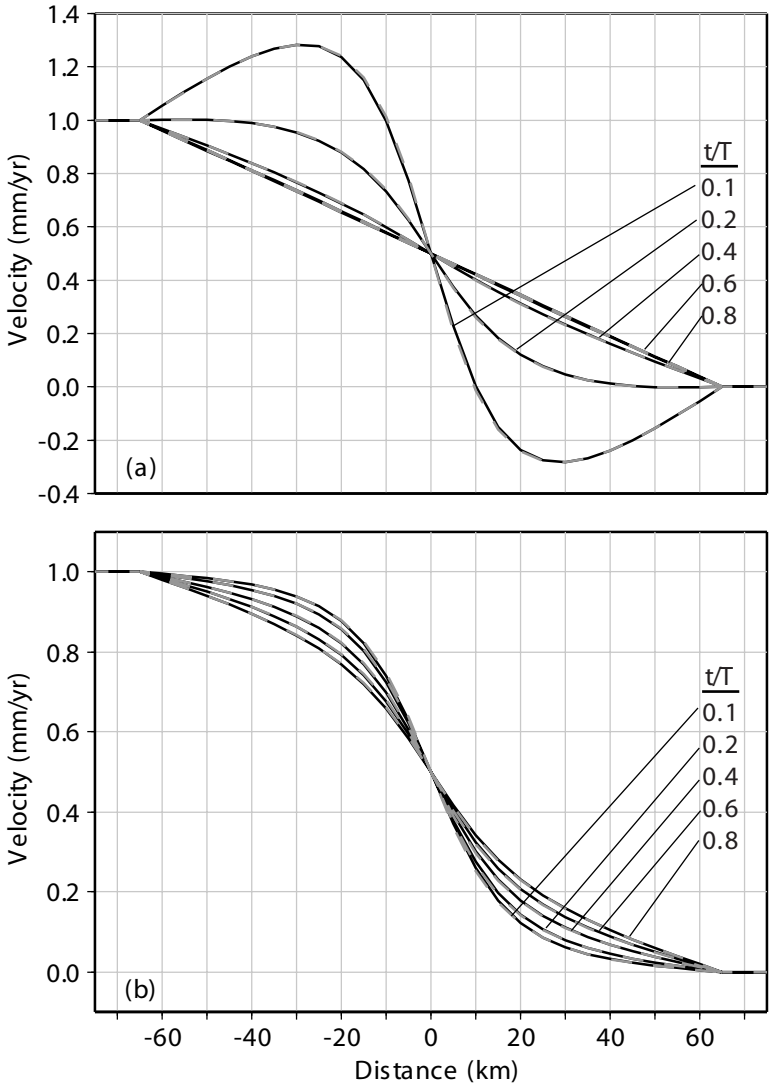
1.4
1.2
1.0
0.8
0.6
0.4
0.2
0.0
-0.2
-0.4
Velocity (mm/yr)
t/T
0.1
0.2
0.4
0.6
0.8
(a)
1.0
0.8
0.6
0.4
0.2
0.0
Velocity (mm/yr)
t/T
0.1
0.2
0.4
0.6
0.8
(b)
-60
-40
-20
0
20
40
60
Distance (km)

Figure 9

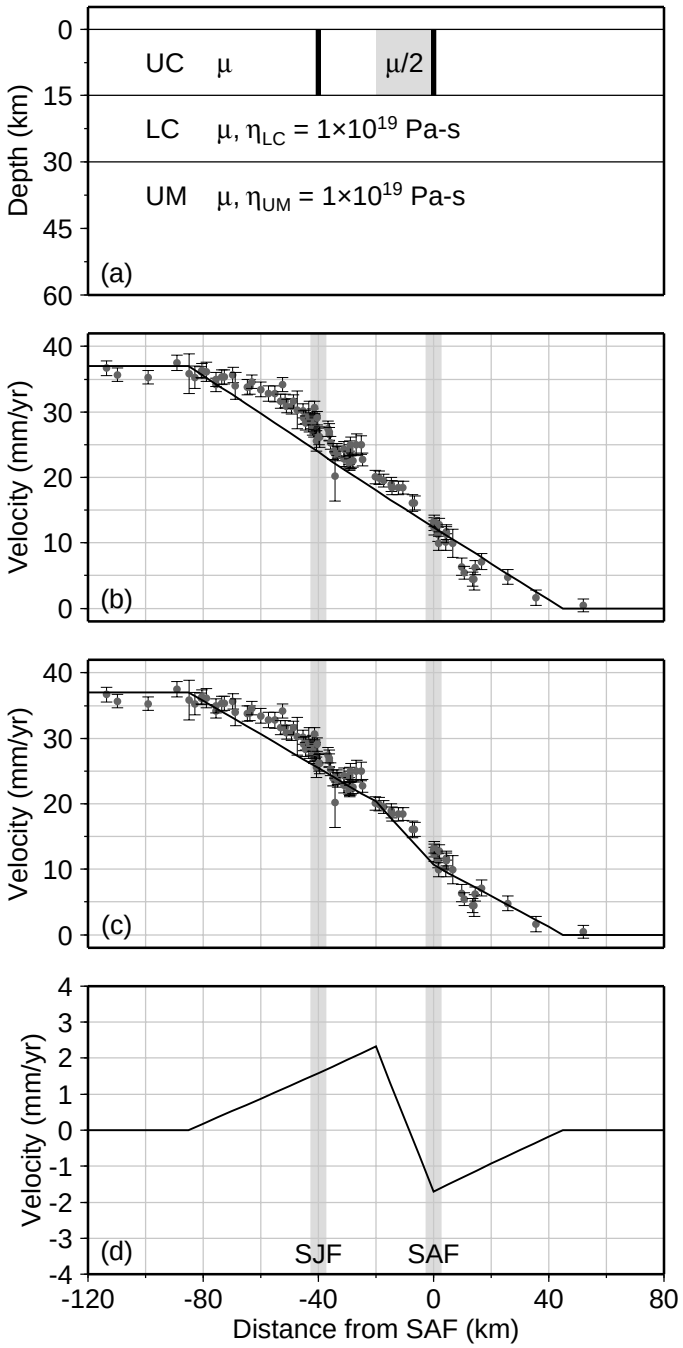
Depth (km)
0
15
30
45
60
UC μ
μ/2
LC μ, η_{LC} = 1×10^{19} Pa-s
UM μ, η_{UM} = 1×10^{19} Pa-s
(a)
Velocity (mm/yr)
40
30
20
10
0
(b)
Velocity (mm/yr)
40
30
20
10
0
(c)
Velocity (mm/yr)
4
3
2
1
0
-1
-2
-3
-4
(d)
SJF
SAF
-120
-80
-40
0
40
80
Distance from SAF (km)

Figure 10

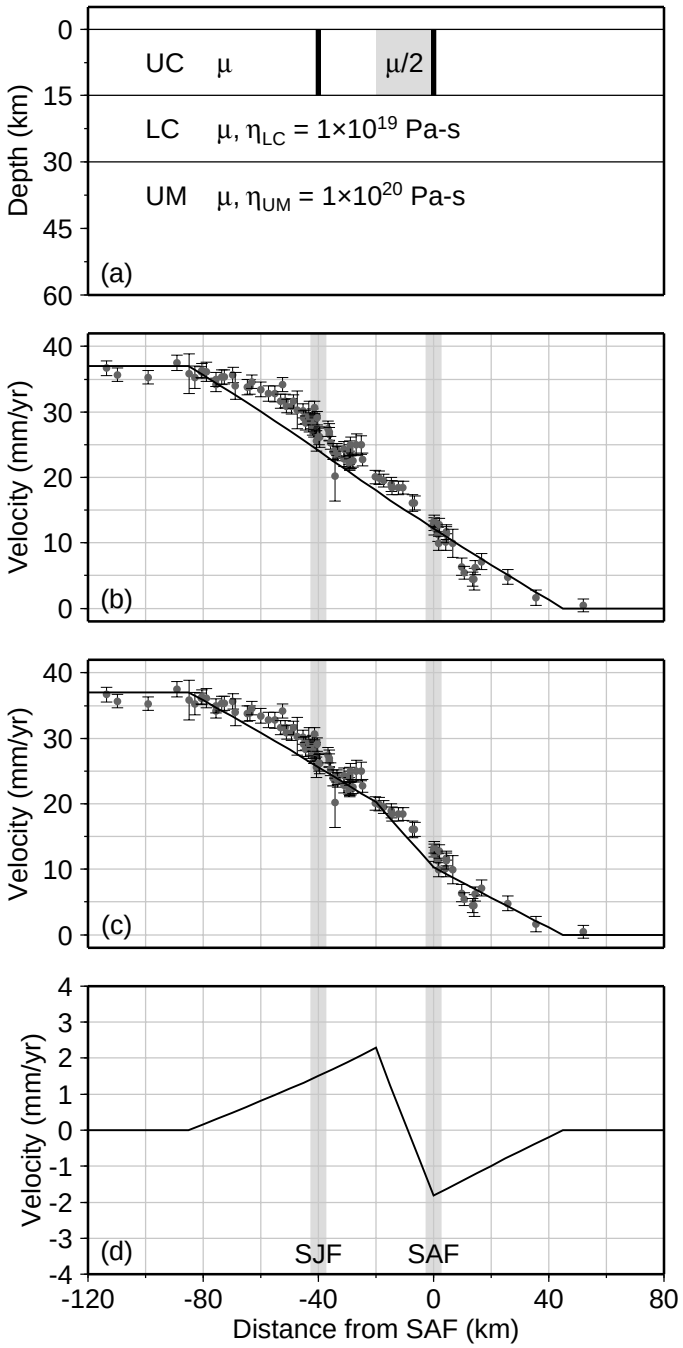
Depth (km)
0
15
30
45
60
UC μ
μ/2
LC μ, η_{LC} = 1×10^{19} Pa-s
UM μ, η_{UM} = 1×10^{20} Pa-s
(a)
Velocity (mm/yr)
40
30
20
10
0
(b)
Velocity (mm/yr)
40
30
20
10
0
(c)
Velocity (mm/yr)
4
3
2
1
0
-1
-2
-3
-4
(d)
SJF
SAF
-120
-80
-40
0
40
80
Distance from SAF (km)

Figure 11

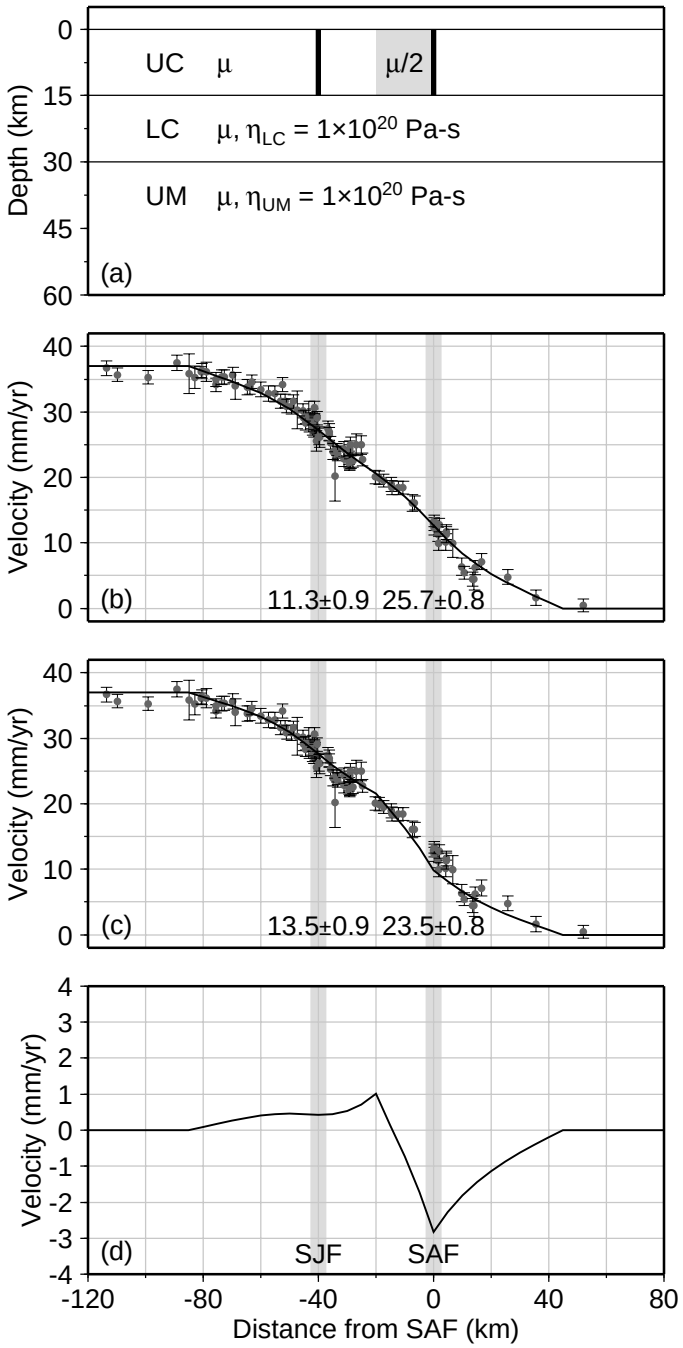
Depth (km)
UC μ
μ/2
LC μ, η_LC = 1×10^20 Pa-s
UM μ, η_UM = 1×10^20 Pa-s
(a)
Velocity (mm/yr)
(b)
11.3±0.9 25.7±0.8
(c)
13.5±0.9 23.5±0.8
(d)
SJF
SAF
Distance from SAF (km)

Figure 12

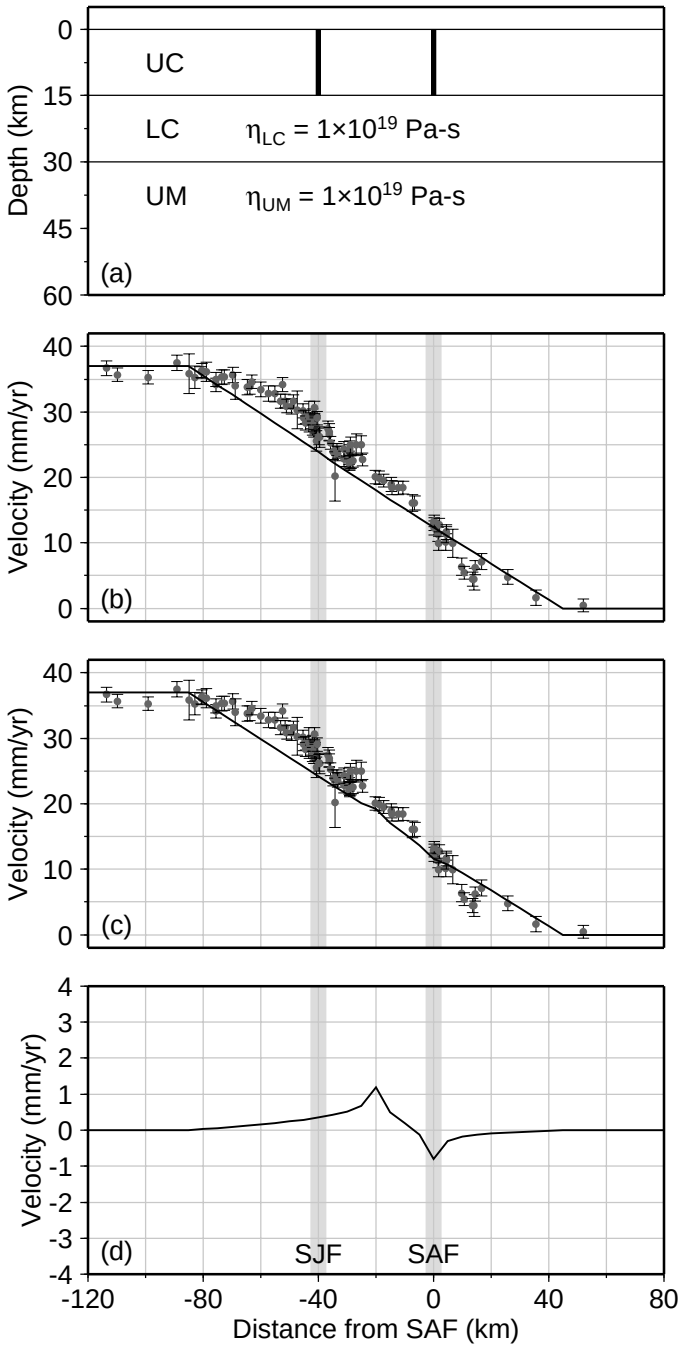
Depth (km)
0
15
30
45
60
UC
LC
UM
η_{LC} = 1×10^{19} Pa-s
η_{UM} = 1×10^{19} Pa-s
(a)
Velocity (mm/yr)
40
30
20
10
0
(b)
Velocity (mm/yr)
40
30
20
10
0
(c)
Velocity (mm/yr)
4
3
2
1
0
-1
-2
-3
-4
(d)
SJF
SAF
-120
-80
-40
0
40
80
Distance from SAF (km)

Figure 13

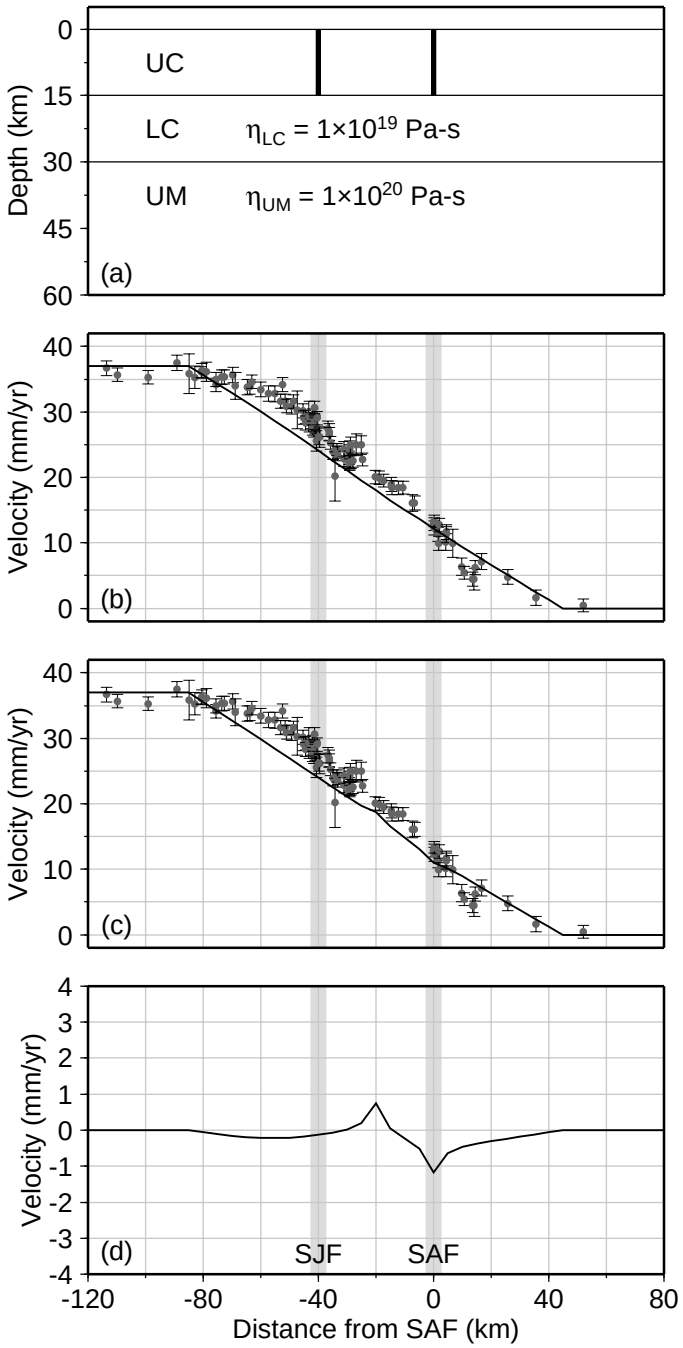
Depth (km)
0
15
30
45
60
UC
LC
UM
η_{LC} = 1×10^{19} Pa-s
η_{UM} = 1×10^{20} Pa-s
(a)
Velocity (mm/yr)
40
30
20
10
0
(b)
Velocity (mm/yr)
40
30
20
10
0
(c)
Velocity (mm/yr)
4
3
2
1
0
-1
-2
-3
-4
(d)
SJF
SAF
-120
-80
-40
0
40
80
Distance from SAF (km)

Figure 14

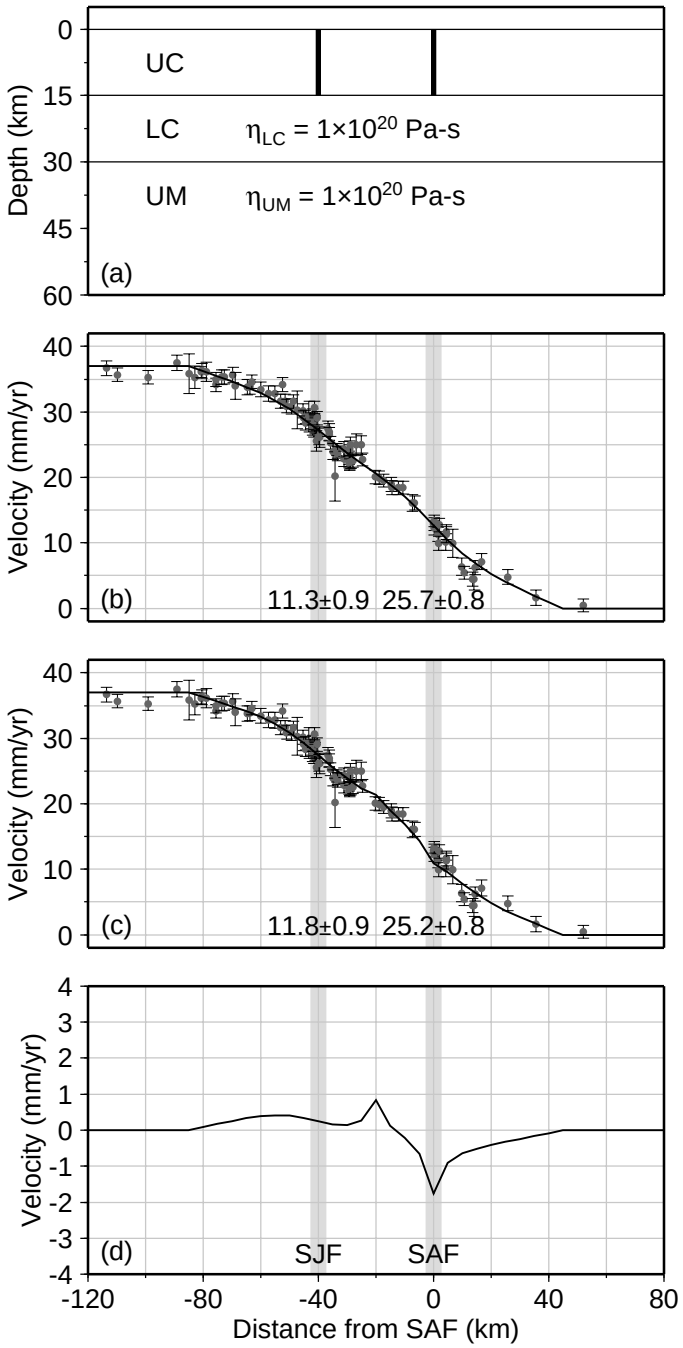
Depth (km)
0
15
30
45
60
UC
LC
η_{LC} = 1×10^{20} Pa-s
UM
η_{UM} = 1×10^{20} Pa-s
(a)
Velocity (mm/yr)
40
30
20
10
0
(b)
11.3±0.9
25.7±0.8
(c)
11.8±0.9
25.2±0.8
4
3
2
1
0
-1
-2
-3
-4
(d)
SJF
SAF
-120
-80
-40
0
40
80
Distance from SAF (km)

Figure 15